Eurographics Conference on Visualization (EuroVis) 2019
M. Gleicher, H. Leitte, and I. Viola
(Guest Editors)

Volume 38 (2019), Number 3

Towards Glyphs for Uncertain Symmetric Second-Order Tensors

Tim Gerrits, Christian Rössl, and Holger Theisel

University of Magdeburg, Germany

Abstract

Measured data often incorporates some amount of uncertainty, which is generally modeled as a distribution of possible samples. In this paper, we consider second-order symmetric tensors with uncertainty. In the 3D case, this means the tensor data consists of 6 coefficients – uncertainty, however, is encoded by 21 coefficients assuming a multivariate Gaussian distribution as model. The high dimension makes the direct visualization of tensor data with uncertainty a difficult problem, which was until now unsolved. The contribution of this paper consists in the design of glyphs for uncertain second-order symmetric tensors in 2D and 3D. The construction consists of a standard glyph for the mean tensor that is augmented by a scalar field that represents uncertainty. We show that this scalar field and therefore the displayed glyph encode the uncertainty comprehensively, i.e., there exists a bijective map between the glyph and the parameters of the distribution. Our approach can extend several classes of existing glyphs for symmetric tensors to additionally encode uncertainty and therefore provides a possible foundation for further uncertain tensor glyph design. For demonstration, we choose the well-known superquadric glyphs, and we show that the uncertainty visualization satisfies all their design constraints.

CCS Concepts

• ***Human-centered computing*** → *Scientific visualization;*

1. Introduction

Uncertainty visualization is one of the current challenges in Scientific Visualization. Modern visual data analysis does not only focus on properties, features, and correlations in the data but also on their uncertainties. This additional consideration comes with a significant increase of data to be processed and visualized: instead of scalar/vector/tensor samples at domain points, either ensembles of scalar/vector/tensor samples or distribution functions have to be processed. The data considered here are *3D uncertain symmetric second order tensor* fields under the assumption of a *normal distribution*. These fields are usually obtained from ensembles of tensor fields, which consist of multiple measurements of a tensor per grid point. Such an uncertain symmetric tensor is represented by a mean tensor (consisting of 6 coefficients) and – after embedding the tensors into a 6D vector space – by a 6×6 covariance matrix (consisting of 21 coefficients).

We present a generic approach to designing glyphs that represent both simultaneously the 6 coefficients of the mean tensor and the 21 coefficients of the covariance matrix. The construction starts from some established glyph representation for the mean tensor by a closed glyph surface. We show that the information encoded in the covariance matrix can be captured by a scalar field that lives on the glyph surface. The scalar function encodes the local perturbation of the glyph surface under applying a normal random perturbation to the mean tensor, where the latter perturbation of the mean tensor is modeled by the covariance matrix. We demonstrate this by visualizing the scalar field as an offset surface to the surface that represents the mean glyph. This provides an understanding of the impact of perturbations to the geometry of the mean glyph or equivalently its likely shape variation under the given uncertainty distribution function. We show that our new glyph uniquely encodes the covariance matrix if the chosen mean glyph is "complicated enough", which is the case, e.g., for the standard representation by superquadrics. In addition, we can measure the "stability" of the mapping between any uncertain glyph and the associated covariance matrix as a single number. We apply the technique to three standard glyphs for the mean tensor: an ellipsoid representation for positive definite tensors, superquadric glyphs [Kin04, SK10], and the glyphs in [GRT17a] for symmetric tensors. We show that the ellipsoid representation does not give full coverage of the information encoded in the covariance matrix whereas superquadric glyphs do. We provide examples and experiments and apply our technique to ensembles of DT-MRI data and mechanical stress tensors.

Notation

We use bold lowercase letters for vector quantities and bold capital letters for matrices/tensors. We use the following standard nabla operator notation for derivatives of scalar functions $g(\mathbf{s})$ and vector fields $\mathbf{g}(\mathbf{s})$ w.r.t. to a vector $\mathbf{s} = (s_1, \ldots, s_n)$:

$$\nabla_{\mathbf{s}} g = \frac{\partial g}{\partial \mathbf{s}} = \left(\frac{\partial g}{\partial s_1}, \ldots, \frac{\partial g}{\partial s_n} \right)^{\mathrm{T}} \text{ and } \nabla_{\mathbf{s}} \mathbf{g} = \frac{\partial \mathbf{g}}{\partial \mathbf{s}} = \left(\frac{\partial \mathbf{g}}{\partial s_1}, \ldots, \frac{\partial \mathbf{g}}{\partial s_n} \right)^{\mathrm{T}}.$$

Further, we use the Mandel notation, which represents symmetric tensors as vectors and define the operator $\mathbf{v}(\cdot)$ that transforms a symmetric second order $(n \times n)$ tensor $\mathbf{S}$ into a vector. We use $n = 2, 3, 6$ which gives vectors of dimension $3, 6, 21$, respectively, as

$$\begin{aligned}\mathbf{v}(\mathbf{S}) &= (s_{11}, s_{22}, \sqrt{2}\, s_{12})^{\mathrm{T}} \\ \mathbf{v}(\mathbf{S}) &= (s_{11}, s_{22}, s_{33}, \sqrt{2}\, s_{12}, \sqrt{2}\, s_{13}, \sqrt{2}\, s_{23})^{\mathrm{T}} \\ \mathbf{v}(\mathbf{S}) &= (s_{11}, \ldots, s_{66}, \sqrt{2}\, s_{12}, \ldots, \sqrt{2}\, s_{16}, \ldots, \sqrt{2}\, s_{56})^{\mathrm{T}}\end{aligned}$$

where s_{ij} denote the tensor components. Note that $\mathbf{v}(\cdot)$ describes an isometric embedding of the tensor space into $\mathbb{R}^{3/6/21}$, i.e., scalar products and hence distances are preserved. In particular, the following holds:

$$\mathbf{r}^{\mathrm{T}}\, \mathbf{S}\, \mathbf{r} = \mathbf{v}(\mathbf{r}\mathbf{r}^{\mathrm{T}})^{\mathrm{T}} \mathbf{v}(\mathbf{S}) \tag{1}$$

for a symmetric second order tensor $\mathbf{S}$ and a vector $\mathbf{r}$. Further, any rotation $\mathbf{R}$ in domain coordinates acting on a tensor $\mathbf{S}$ corresponds to a rotation $\hat{\mathbf{R}}$ acting on $\mathbf{v}(\mathbf{S})$ in the isomorphic vector space such that

$$\mathbf{v}(\mathbf{R}\, \mathbf{S}\, \mathbf{R}^{\mathrm{T}}) = \hat{\mathbf{R}}\, \mathbf{v}(\mathbf{S})\,. \tag{2}$$

For details on notation and properties see, e.g., [Hel94]. We use the operator $\mathbf{v}(\cdot)$ to describe the uncertainty of second order tensors in terms of standard matrix and vector operations instead of non-standard higher order tensor operations. This was done similarly in [BP03, AWHS16].

2. The visualization problem

We assume an uncertain tensor under normal distribution that is described by the distribution function

$$p(\mathbf{S}) = \frac{1}{\sqrt{(2\pi)^n \det \mathbf{C}}} \exp\{-\tfrac{1}{2} \mathbf{v}(\mathbf{S}-\bar{\mathbf{S}})^{\mathrm{T}}\, \mathbf{C}^{-1}\, \mathbf{v}(\mathbf{S}-\bar{\mathbf{S}})\}\,. \tag{3}$$

This function has two parameters: the mean tensor $\bar{\mathbf{S}}$ and the covariance matrix $\mathbf{C}$, which describes not only the variance of the individual coefficients of $\mathbf{v}(\mathbf{S})$ but also their linear dependencies. So, we define an *uncertain tensor* as a pair $(\bar{\mathbf{S}}, \mathbf{C})$. Note that $\mathbf{C}$ is a symmetric positive definite matrix. In 2D, it is a 3×3 matrix with 6 distinct entries, while in 3D it is a 6×6 matrix with 21 entries.

Assuming a Gaussian distribution to describe uncertainty in tensor data is common and widely accepted in the literature [BP03, BP07, AWHS16]. We remark that alternative models exist and are used in settings, where this assumption does not hold; for instance, [ZSL*16, ZCH*17] use a modified mean tensor.

Given m tensor samples $\mathbf{S}_1, \ldots \mathbf{S}_m$, e.g., from an ensemble data set with m members, the best-fitting uncertain tensor is given by

$$\bar{\mathbf{S}} = \frac{1}{m} \sum_{i=1}^{m} \mathbf{S}_i \quad \text{and} \quad \mathbf{C} = \frac{1}{m} \sum_{i=1}^{m} \mathbf{v}(\mathbf{S}_i - \bar{\mathbf{S}})\, \mathbf{v}(\mathbf{S}_i - \bar{\mathbf{S}})^{\mathrm{T}}\,. \tag{4}$$

We search for glyphs that encode both $\bar{\mathbf{S}}$ and $\mathbf{C}$ and satisfy a list of properties. In order to express these properties we first need to specify the terms *scaled* and *rotated uncertain tensor*. Assume that the same rotation or scaling is applied to all tensor samples in (4). Then scaling by a factor $\rho > 0$ gives the scaled uncertain tensor $(\rho\bar{\mathbf{S}}, \rho^2\mathbf{C})$, and rotation by $\mathbf{R}$ gives the rotated uncertain tensor $(\mathbf{R}\bar{\mathbf{S}}\mathbf{R}^{\mathrm{T}}, \hat{\mathbf{R}}\mathbf{C}\hat{\mathbf{R}}^{\mathrm{T}})$ with $\hat{\mathbf{R}}$). A construction of $\hat{\mathbf{R}}$ from $\mathbf{R}$ is given in the Appendix.

A wish list for uncertain glyphs

Glyph design is a creative process. *The* one and only perfect glyph usually does not exist. A common approach starts with the formulation of desired and/or required properties to constrain the search to conforming glyphs. Our "wish list" of properties is similar to [SK10] and [GRT17a] and their work includes detailed justifications for their importance. Let $(\bar{\mathbf{S}}, \mathbf{C})$ be an uncertain tensor and $G(\bar{\mathbf{S}}, \mathbf{C})$ its glyph representation.

1. *Rotation invariance:* $G(\mathbf{R}\bar{\mathbf{S}}\mathbf{R}^{\mathrm{T}}, \hat{\mathbf{R}}\mathbf{C}\hat{\mathbf{R}}^{\mathrm{T}}) = \mathbf{R}\, G(\bar{\mathbf{S}}, \mathbf{C})$ for any rotation matrices $\mathbf{R}$ and $\hat{\mathbf{R}}$ as in (19).
2. *Scaling invariance:* $G(\rho\bar{\mathbf{S}}, \rho^2\mathbf{C}) = \rho\, G(\bar{\mathbf{S}}, \mathbf{C})$ for a positive scaling factor ρ.
3. *Continuity:* Small changes in tensor or covariance matrix should result in small changes in the glyph: $(\bar{\mathbf{S}}_1, \mathbf{C}_1) \approx (\bar{\mathbf{S}}_2, \mathbf{C}_2) \Rightarrow G(\bar{\mathbf{S}}_1, \mathbf{C}_1) \approx G(\bar{\mathbf{S}}_2, \mathbf{C}_2)$.
4. *Uniqueness*: The glyph should contain information to uniquely reconstruct the uncertain tensor: no two different tensors should have the same glyph representation: $(\bar{\mathbf{S}}_1, \mathbf{C}_1) \neq (\bar{\mathbf{S}}_2, \mathbf{C}_2) \Rightarrow G(\bar{\mathbf{S}}_1, \mathbf{C}_1) \neq G(\bar{\mathbf{S}}_2, \mathbf{C}_2)$.
5. *Direct encoding of real eigenvectors/eigenvalues of* $\bar{\mathbf{S}}$*:* Since the eigenvectors/eigenvalues of $\bar{\mathbf{S}}$ have a well-defined meaning in most applications, they should be directly encoded in G.
6. *Convergence for* $\mathbf{C} \to \mathbf{0}$*:* For vanishing uncertainty, G should converge to a well-defined glyph encoding all information of $\bar{\mathbf{S}}$.
7. *Intuitiveness*: The glyph should be easily readable and should have an intuitive interpretation.

Properties (1.–5.) are direct generalizations of standard glyph properties for the certain case, as formulated in [SK10] and [GRT17a]. Property (6.) requires that the certain case should be a well-defined special case in all uncertain tensor glyphs. Property (7.) is the only one that cannot be shown by a mathematical proof, due to the lack of a mathematical definition of the concept of intuitiveness. The main contribution of this paper is to *prove* that our glyphs fulfill the properties (1.–6.). We should search for intuitive glyphs in the subspace of all possible glyphs given by properties (1.–6.).

3. Related Work

This work extends current glyph-based visualization techniques for second-order tensors by additionally encoding uncertainty. Both, tensor visualization as well as uncertainty visualization, form their own fields of research with many contributions over the last years. This section summarizes a selection of contributions.

3.1. Tensor Glyphs

Second-order tensors are used in a large variety of applications, i.e., for modeling stress, diffusion or fluid flow. Glyphs have been proven to be a powerful visualization tool for such data. Every tensor can be decomposed into a unique set of eigenvectors and eigenvalues, which enable the mapping of tensor invariants to geometric properties like size, shape, orientation or color. Kindlmann introduced

superquadrics as glyphs [Kin04] as an intuitive visualization tool for diffusion tensors. Such tensors are symmetric, i.e., their eigenvectors are orthogonal, and positive-definite, i.e., their eigenvalues are positive. Schultz extended this work for indefinite symmetric tensors [SK10]. Both works give an extensive overview of further techniques for visualizing symmetric second-order tensors.

Vector field Jacobians provide an example of tensor fields that are generally non-symmetric. This means eigenvectors are generally non-orthogonal, and eigenvalues/eigenvectors may be non-real. Seltzer et al. [SK16] introduce glyphs for asymmetric second-order 2D tensors, where texture is used to encode rotational behavior. Gerrits et al. [GRT17a] introduce a different glyph construction technique for general second-order tensors in 2D and 3D that is based on strict visualization principles, similar to our wish list given in Section 2. This work was extended to glyphs that represent time-dependent vector field Jacobians by finding a suitable mapping of the time-derivative into the visualization space [GRT17b].

3.2. Uncertainty Visualization

Uncertainty in data describes how reliable or useful these data are. Modeling and considering uncertainty is critical in many applications including medical imaging or optimization and decision making based on mechanical simulations or computational fluid dynamics. Its visualization is a key to understanding (sources of) uncertainty and to properly define policies in the presence of uncertainty. Visualizing uncertainty is generally a challenging task, as it adds another dimension to the visualization space. There exists a multitude of approaches to uncertainty visualization, see, e.g., the reviews by Bonneau et al. [BHJ*14] and Brodlie et al. [BOL12].

3.3. Uncertain Tensors

This work aims at visualizing uncertainty in tensor data. A notorious example for such data are diffusion tensors, which are obtained, e.g., from diffusion tensor magnetic resonance imaging (DT-MRI). Uncertainty typically stems from the measurement process, which introduces a significant amount of Gaussian noise [BP03]. An alternative source of uncertainty is fusion of tensors from members of an ensemble.

Several approaches deal with visualizing the uncertainty in tensor fields by considering not the whole tensor and its uncertainty but only derived scalar and vector invariants. Jones introduced the *cones of uncertainty* [Jon03] to encode the local variance of eigenvector estimates. This provides a confidence visualization, but fails to show distributions as unique glyphs. Schultz et al. [SSSSW13] provide a new glyph that aims at a more detailed understanding of the distribution of fiber variability from DT-MRI. The construction is based on decomposing the probability measure into a main direction and a residual, combining both into what they call the *HiFiVE* glyph.

Jiao et al. [JPGJ12] compute what they call SIP glyphs from orientation distribution functions and volume rendering of a large number of samples from the distribution. The volume data that results from superimposing these renderings can visualize the shape inclusion probability (SIP, see [LP09]) gives one possible geometric interpretation of uncertainty. This approach is related to ours because it is driven by geometry and even some of their glyphs may appear similar to ours. However, its is also very different: Firstly, it lacks of (provable) adherence to design principles summarized in the previous section, e.g., directions of eigenvectors or magnitude of eigenvalues of the mean tensor may not be directly visualized. Secondly, the glyph encodes the uncertainty in a 3D scalar field, while our approach encodes the uncertainty in a 2D scalar field on the glyph surface. Finally, its glyph computation is based on generating a large number of random samples, which are "fused" to a glyph representation. In contrast, our approach constructs a well-defined shape as a parametric or implicit function.

Basser et al. [BP03, BP07] suggest two visualizations: First, they propose visualizing the covariance matrix independently of the mean tensor. While this provides a useful representation of the covariance itself, it raises a number of problems. Firstly, the same covariance matrix shows different impact on different mean tensors. Secondly, only a subset of the full covariance matrix is visualized. Thirdly, this visualization is not invariant under rotation of the coordinate system or tensors, respectively. Their second visualization proposes showing the mean tensor and its variance as three isosurfaces representing mean and standard deviation. Even though, this is a first approach to visualizing the impact of the covariance matrix on the mean tensor, only the totally symmetric part of the covariance is used, resulting in a violation of property (4.). These shortcomings are discussed in [AWHS16]. Based on these observations, Abbasloo et al. [AWHS16] provide another solution: The main idea is to consider a spectral analysis and to visualize the tensor perturbations in the directions of the 6 eigenvectors of the covariance matrix. Then the whole covariance matrix is covered by a simultaneous observation of 6 tensor deformations. While this gives a complete picture of the uncertain tensor, it does not satisfy the continuity property (3.): if two eigenvalues of the covariance tensor get close to each other, the corresponding eigenvectors (and therefore the 6 visualizations) may show discontinuities. In a similar approach for ensembles of tensor data, Zhang et al. [ZCH*17] provide a framework to combine several visualizations to gain a general overview of the whole ensemble, as well as a detailed information of distinct tensor properties. They divide uncertainty in three independent parts (scaling, shape and rotation) and encode each with one variance number. This way, the glyphs they propose encode only a 3-dimensional subspace of the complete 21-dimensional space spanned by an uncertain tensor.

The following table compares existing work on uncertain symmetric tensor glyphs with respect to the design properties (1.–6.). The additional last column (±) indicates, whether the glyph visualization distinguishes between indefinite and definite general symmetric second-order tensors. Properties that could not be decided are indicated as "?".

method / satisfies	(1.)	(2.)	(3.)	(4.)	(5.)	(6.)	±
[Jon03]	✓	✓	✗	✗	?	?	✗
[BP07]	✓	✓	✓	✓	✗	✓	✗
[JPGJ12]	✓	✓	✓	✗	?	✓	✗
[SSSSW13]	✓	✓	✗	✗	?	?	✗
[AWHS16]	✓	✓	✗	✓	✗	✓	✓
[ZCH*17]	✓	✓	✗	✗	✓	✓	✗
Ours: ellipsoid	✓	✓	✓	✗	✓	✓	✗
Ours: superquadric	✓	✓	✓	✓	✓	✓	✓
Ours: [GRT17a]	✓	✓	✓	✓	✓	✓	✓

We conclude this review of related work with the statement that – to the best of our knowledge – no glyph for uncertain tensors exists that fulfills properties (1.–6.). Moreover, [AWHS16] even state that due to the high data complexity, "*it does not seem promising to try and visualize all aspects of tensor covariance simultaneously*". We disagree with this statement and propose a solution to this visualization problem in the following.

4. Glyphs for Uncertain Symmetric Tensors

We propose a generic approach that extends any glyph definition for a "certain" tensor $\mathbf{S}$ to the uncertain case to provide a glyph for $(\bar{\mathbf{S}}, \mathbf{C})$. A variety of glyph definitions exist for the certain case. These glyphs are often described as closed surfaces (or curves in 2D), sometimes with additional color information. A glyph surface is either given in *implicit* form

$$g(\mathbf{S}, \mathbf{x}) = 0 \tag{5}$$

or in *parametric* form

$$\mathbf{g}(\mathbf{S}, \theta, \phi)\ , \tag{6}$$

with surface parametrization (θ, ϕ). For the uncertain case, we represent the mean tensor by a standard glyph surface. In addition, we define a non-negative scalar field q on the glyph surface that encodes the impact of the covariance $\mathbf{C}$ on $\bar{\mathbf{S}}$. We write q short for $q(\mathbf{S}, \mathbf{x})$ (for $g(\mathbf{S}, \mathbf{x}) = 0$) and $q(\mathbf{S}, \theta, \phi)$, likewise, and define

$$q = \sqrt{\mathbf{q}^{\mathrm{T}}\, \mathbf{C}\, \mathbf{q}} \tag{7}$$

with

$$\mathbf{q} = \mathbf{q}(\mathbf{S}, \mathbf{x}) = \frac{\nabla_{\mathbf{s}}\, g}{||\nabla_{\mathbf{x}}\, g||} \tag{8}$$

for the implicit case and

$$\mathbf{q} = \mathbf{q}(\mathbf{S}, \theta, \phi) = (\nabla_{\mathbf{s}}\, \mathbf{g})\mathbf{n} \tag{9}$$

for the parametric case with $\mathbf{s} = \mathbf{v}(\mathbf{S})$, and $\mathbf{n} = \frac{1}{||\cdot||}\left(\frac{\partial \mathbf{g}}{\partial \theta} \times \frac{\partial \mathbf{g}}{\partial \phi}\right)$ is the surface normal. Note that for the implicit case, $\nabla_{\mathbf{s}}\, g$ is a 3-vector in 2D and a 6-vector in 3D. For the parametric case, $\nabla_{\mathbf{s}}\mathbf{g}$ is a 3×2 matrix in 2D and a 6×3 matrix in 3D.

Derivation and Explanation

In order to explain the idea of the field q, we consider the concept of *normal velocity of a time-dependent surface*. Assume a time-dependent surface either in an implicit representation $g(\mathbf{x}, t) = 0$ or in a parametric representation $\mathbf{g}(\theta, \phi, t)$. The surface changes shape and location under variation of the time parameter t. The normal velocity of the surface describes the change of the surface in the direction of the surface normal as

$$r = -\frac{g_t}{||\nabla_{\mathbf{x}}\, g||} \tag{10}$$

for the implicit case and with $g_t = \frac{\partial g}{\partial t}$ for the implicit case and

$$r = \frac{\partial \mathbf{g}}{\partial t}^{\mathrm{T}} \mathbf{n} = \mathbf{g}_t{}^{\mathrm{T}} \mathbf{n} \tag{11}$$

with $\mathbf{g}_t = \frac{\partial \mathbf{g}}{\partial t}$ for the parametric case. Figure 1 gives an illustration.

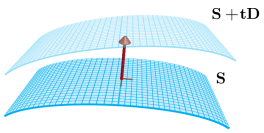

Figure 1: *The normal velocity r of a time-dependent surface.*

Returning to tensors, we observe how a glyph surface behaves under a perturbation

$$\mathbf{S} \to \mathbf{S} + t\, \mathbf{D} \tag{12}$$

to the tensor for a small t. We want to observe the directional derivative of $\mathbf{v}(\mathbf{S})$ in the direction $\mathbf{v}(\mathbf{D})$. We do so by considering the time-dependent surfaces

$$g(\mathbf{v}(\mathbf{S}) + t\, \mathbf{v}(\mathbf{D}), \mathbf{x}) = 0 \quad \text{and} \quad \mathbf{g}(\mathbf{v}(\mathbf{S}) + t\, \mathbf{v}(\mathbf{D}), \theta, \phi)\ .$$

Computing their normal velocity for $t = 0$ gives

$$r(\mathbf{S}, \mathbf{D}, \mathbf{x}) = -\mathbf{v}(\mathbf{D})^{\mathrm{T}} \mathbf{q} \tag{13}$$

with $\mathbf{q}$ as defined in (8) for the implicit case and

$$r(\mathbf{S}, \mathbf{D}, \theta, \phi) = \mathbf{v}(\mathbf{D})^{\mathrm{T}} \mathbf{q} \tag{14}$$

with $\mathbf{q}$ as defined in (9) for the parametric case.

Equations (13) and (14) describe the normal velocity of the glyph surface under a *particular* perturbation $\mathbf{D}$. In order to consider the behavior of the glyph surface under *all* possible perturbations, we consider r^2 as

$$r^2 = \mathbf{q}^{\mathrm{T}} \mathbf{v}(\mathbf{D})\, \mathbf{v}(\mathbf{D})^{\mathrm{T}} \mathbf{q}, \tag{15}$$

and replace $\mathbf{v}(\mathbf{D})\, \mathbf{v}(\mathbf{D})^{\mathrm{T}}$ by the covariance matrix $\mathbf{C}$. This gives $q = \sqrt{r^2}$ as defined in (7). So the field q describes the mean absolute values of the normal velocities of an arbitrary glyph surface perturbation $\mathbf{D}$ with the distribution of $\mathbf{D}$ given by $\mathbf{C}$.

Computation and Visualization

Although the computation of q by (7)–(9) is conceptually simple, the concrete implementation becomes involved for glyph representations that require a spectral decomposition of the tensor: In this case, the derivatives of the decomposition with respect to the glyph components need to be computed, which is difficult and generally unpractical in closed-from. However, the algorithmic computation of q is indeed simple if derivatives are approximated numerically by finite differences. This is what we use in our implementation. One potential pitfall remains: Care has to be taken when different parametric representations exist for the same tensor (i.e.the superquadric glyphs). In this case we have to ensure that the same parametrization is used for all samples required for estimating a derivative.

For visualization, we render two closed surfaces: the mean glyph surface G, and a surface Q defined as $Q = G + q\,\mathbf{n}$ where $\mathbf{n}$ is the surface normal on G. This means that Q is a scaled offset surface of G where q dictates the normal distance between G and Q. The joint

visualization of the two nested surfaces G and Q is a standard problem for visualization. Here, we apply a straightforward rendering using semi-transparency.

A special case that should be considered consists in a mean glyph surface G that is C^0 continuous at certain locations, i.e., sharp edges or corners. These locations result in a locally discontinuous Q, i.e., a surface with boundaries at "jumps". This can happen at single points as well as along a closed line. We close such boundary loops with ruled surfaces to maintain a closed surface. At singularities, where different values can be mapped to the same point, we chose to set the offset to zero.

5. Analysis

In this section we show that the proposed glyphs fulfill properties (1.-7). Properties (1.,2.,3.,5). are generic properties. If they are fulfilled by the underlying glyph for the mean tensor, equations (7)–(9) ensure that they carry over directly to the glyph for the uncertain tensor. Property (6.) is simple: (7) gives that for $\mathbf{C} \to \mathbf{0}$, we get $q \to 0$ and therefore convergence to the "certain" glyph .

Properties (4., uniqueness), and (7., intuitiveness) are harder to show. Uniqueness is not generic: different choices of glyphs for mean tensor result in different statements about uniqueness.

5.1. Uniqueness

To prove or counter-prove the uniqueness of a glyph for an uncertain tensor $(\bar{\mathbf{S}}, \mathbf{C})$, we assume that the mean tensor $\bar{\mathbf{S}}$ is uniquely represented by the glyph surface itself. It remains to show that all 21 coefficients of $\mathbf{C}$ can be uniquely derived from the scalar field q on the glyph surface. In fact, to show uniqueness, we have to show that there exist 21 sample points $\mathbf{g}_1, \dots, \mathbf{g}_{21}$ on the glyph surface such that the corresponding samples $q_1, \dots, q_{21}$ of the field $q(\mathbf{g})$ enables a unique reconstruction of the covariance matrix $\mathbf{C}$. Let $\mathbf{q}_1, \dots, \mathbf{q}_{21}$ denote the corresponding samples of the vector field $\mathbf{q}$ given in (7) such that $q_i^2 = \mathbf{q}_i^{\mathrm{T}} \mathbf{C}\, \mathbf{q}_i$. Then (1) and (7) give

$$(q_1^2, \dots, q_{21}^2)^{\mathrm{T}} = \mathbf{M}^{\mathrm{T}} \mathbf{v}(\mathbf{C}) \tag{16}$$

with

$$\mathbf{M} = \left(\mathbf{v}(\mathbf{q}_1 \mathbf{q}_1^{\mathrm{T}}), \dots, \mathbf{v}(\mathbf{q}_{21} \mathbf{q}_{21}^{\mathrm{T}}) \right) \in \mathbb{R}^{21 \times 21}. \tag{17}$$

In order to show that $\mathbf{v}(\mathbf{C})$ can be computed from $(q_1^2, \dots, q_{21}^2)^{\mathrm{T}}$ (and vice versa), we have to show that $\mathbf{M}$ has full rank for the chosen sample points.

Equations (16) and (17) show that the uniqueness of a glyph depends on the behavior of $\mathbf{q}$ on the glyph surface. Let $\mathcal{Q}$ be the *set of all vectors* $\mathbf{q}$ *on the glyph surface*. A characterization of $\mathcal{Q}$ is the key to study uniqueness.

Lemma 1. *An uncertain glyph is* not *unique iff all* $\mathbf{q} \in \mathcal{Q}$ *live on a common quadric,i.e., there exists a non-zero matrix* $\mathbf{A}$ *such that* $\mathbf{q}^{\mathrm{T}} \mathbf{A}\, \mathbf{q} = 0$ *for all* $\mathbf{q} \in \mathcal{Q}$.

In order to prove the lemma we first show that a glyph is *not* unique if such matrix exists. Assume that there exists a non-zero matrix $\mathbf{A}$ that fulfills $\mathbf{q}^{\mathrm{T}} \mathbf{A}\, \mathbf{q} = 0$ for all $\mathbf{q} \in \mathcal{Q}$. Then for any selection of sample points $\mathbf{g}_1, \dots, \mathbf{g}_{21}$ we have $\mathbf{q}_i^{\mathrm{T}} \mathbf{A}\, \mathbf{q}_i = 0$ for $i = 1, \dots, 21$. Writing this in matrix form using (1) gives

$$\mathbf{M}^{\mathrm{T}}\, \mathbf{v}(\mathbf{A}) = \mathbf{0}_{21} \tag{18}$$

with $\mathbf{M}$ as in (17). Since $\mathbf{v}(\mathbf{A})$ is non-zero, (18) can only hold if $\mathbf{M}^{\mathrm{T}}$ has a zero eigenvalue with the corresponding eigenvector $\mathbf{v}(\mathbf{A})$. Therefore, $\mathbf{M}$ has a rank deficit for any selection of sample points, there is no unique solution to (16), and therefore the uncertain glyph is not unique.

For the reverse direction, we assume that an uncertain glyph is *not* unique, i.e., we have chosen sample points $\mathbf{g}_1, \dots, \mathbf{g}_{21}$ such that the matrix $\mathbf{M}$ is singular. Then there exists a (non-zero) eigenvector $\mathbf{v}(\mathbf{E})$ that corresponds to a zero eigenvalue, i.e., $\mathbf{M}^{\mathrm{T}} \mathbf{v}(\mathbf{E}) = \mathbf{0}_{21}$. Due to (1) and the definition of $\mathbf{M}$ (17), the latter condition is equivalent to

$$\mathbf{v}(\mathbf{q}_i \mathbf{q}_i^{\mathrm{T}})^{\mathrm{T}} \mathbf{v}(\mathbf{E}) = \mathbf{q}_i^{\mathrm{T}} \mathbf{E}\, \mathbf{q}_i = 0 \quad \text{for } i = 1, \dots, 21 \,,$$

which implies that the samples live on the common quadric defined by $\mathbf{E}$. □

With help of lemma 1, we can now analyze particular uncertain tensor glyphs:

Theorem 1. *Uncertain* ellipsoid glyphs *for positive definite tensors are* not *unique.*

We summarize the proof of theorem 1 for uncertain tensors in 2D. The general construction is identical for the 3D case, however, the generated expressions are significantly more complex.

Given is an uncertain tensor $(\bar{\mathbf{S}}, \mathbf{C})$ with $\mathbf{v}(\bar{\mathbf{S}}) = \mathbf{s}$. The surface of the ellipsoid glyph of the mean tensor is given as implicit surface $g(\bar{\mathbf{S}}, \mathbf{x}) = 0$ with $g(\bar{\mathbf{S}}, \mathbf{x}) = \mathbf{x}^{\mathrm{T}} \bar{\mathbf{S}}^{-2} \mathbf{x} - 1$ or equivalently as the image $\{ \mathbf{S}\mathbf{x} \,|\, \mathbf{x}^{\mathrm{T}} \mathbf{x} = 1 \}$. We want to show that for this choice of g there exists an $\mathbf{A} \neq \mathbf{0}$ such that $\mathbf{q}^{\mathrm{T}} \mathbf{A} \mathbf{q} = 0$, which is equivalent to $(\nabla_{\mathbf{s}} g)^{\mathrm{T}} \mathbf{A} \nabla_{\mathbf{s}} g = 0$ after dropping the normalization. Let $\mathbf{x} = (x_1, x_2)$ with $||x||^2 = x_1^2 + x_2^2 = 1$. Then the evaluation of the gradient at a surface point gives

$$\nabla_{\mathbf{s}} g(\bar{\mathbf{S}}, \mathbf{S}\mathbf{x}) = \frac{2}{2 s_{11} s_{22} - s_{12}^2} \begin{pmatrix} (2 s_{22} x_1 - \sqrt{2} s_{12} x_2) x_1 \\ (\sqrt{2} s_{12} x_1 - 2 s_{11} x_2) x_2 \\ s_{12} - \sqrt{2}(s_{11} + s_{22}) x_1 x_2 \end{pmatrix},$$

and for the further consideration we can drop the factor that is constant in $\mathbf{x}$. The remaining expression

$$\tilde{\mathbf{q}} := (s_{11} s_{22} - \tfrac{1}{2} s_{12}^2) \cdot \nabla_{\mathbf{s}} g(\bar{\mathbf{S}}, \mathbf{S}\mathbf{x})$$

is linear in $\mathbf{s}$, and we can write

$$\tilde{\mathbf{q}} = \mathbf{B}\mathbf{r} := \begin{pmatrix} 2 s_{22} & 0 & -\sqrt{2} s_{12} \\ 0 & -2 s_{11} & \sqrt{2} s_{12} \\ s_{12} & s_{12} & -\sqrt{2}(s_{11} + s_{22}) \end{pmatrix} \begin{pmatrix} x_1^2 \\ x_2^2 \\ x_1 x_2 \end{pmatrix}.$$

We will now show that the glyph is not unique by lemma 1 and use the fact that the above matrix $\mathbf{B}$ has full rank and is invertible.

We have $q^2 = \varphi\, \tilde{\mathbf{q}}^{\mathrm{T}} \tilde{\mathbf{q}}$ for some factor $\varphi \neq 0$ that is constant in $\mathbf{x}$, i.e., independent of the chosen surface point. Consider the vector $\mathbf{r}$ and find a matrix $\mathbf{T} \neq \mathbf{0}$ such that $\mathbf{r}^{\mathrm{T}} \mathbf{T}\, \mathbf{r} = 0$. In this case there are

three distinct choices up to scaling, e.g.,

$$\mathbf{T} = \begin{pmatrix} 0 & \frac{1}{2} & 0 \\ \frac{1}{2} & 0 & 0 \\ 0 & 0 & -1 \end{pmatrix}.$$

We use that $\mathbf{B}$ is invertible in order to construct $\mathbf{A} = \mathbf{B}^{-\mathrm{T}}\mathbf{T}\mathbf{B}^{-1}$, which is similar to $\mathbf{T}$, and for which $\varphi^{-1}\mathbf{q}^{\mathrm{T}}\mathbf{A}\mathbf{q} = \tilde{\mathbf{q}}^{\mathrm{T}}\mathbf{A}^{\mathrm{T}}\tilde{\mathbf{q}} = \mathbf{r}^{\mathrm{T}}\mathbf{B}^{-\mathrm{T}}\mathbf{T}\mathbf{B}^{-1}\mathbf{r} = \mathbf{r}^{\mathrm{T}}\mathbf{T}\mathbf{r} = 0$ for all $\mathbf{r}$ and therefore also for all $||\mathbf{x}|| = 1$ and all surface points $\mathbf{S}\mathbf{x}$, respectively. With lemma 1 this proves the theorem. □

Theorem 2. *Uncertain* superquadric glyphs *for positive definite tensors are unique if all eigenvalues of the mean tensor are nonzero and distinct.*

We sketch a proof of this theorem for the 2D case in the Appendix. The basic idea of the proof is simple: find 6 samples of points on the glyph surface such that the matrix $\mathbf{M}$ (17) has full rank. The difficulty of the proof consists in the fact that the construction of superquadrics involves a change of coordinates using the spectral basis of the mean tensor $\bar{\mathbf{S}}$, i.e., it is parametrized by eigenvalues and eigenvectors, whereas partial derivatives must be computed w.r.t. the entries $\mathbf{v}(\bar{\mathbf{S}})$.

Quantifying uniqueness

As mentioned above, a formal proof that a new uncertain glyph is unique can be difficult. The reason is that many glyph definitions – like the superquadric glyphs – rely on the spectral decomposition of the tensor. This makes finding a formal proof seemingly the hardest task when establishing a new glyph for uncertain tensors – significantly harder than the definition and implementation.

To cope with this, we introduce a measure of the "uniqueness" of an uncertain glyph: we measure how stably the covariance matrix $\mathbf{C}$ can be reconstructed from m samples ($m \geq 21$) $q_1, \ldots, q_m$ of the function q at the sample points $\mathbf{g}_1, \ldots, \mathbf{g}_m$ on the glyph surface G. In the ideal case, a small perturbation in $\mathbf{C}$ results in small changes in $q_1, .., q_m$, and vice versa. The reconstruction of q from $\mathbf{C}$ is defined by the linear mapping (16) if $m = 21$. For $m > 21$ samples, the map is given by the corresponding least-squares solution to

$$\mathbf{M}\mathbf{M}^{\mathrm{T}}\mathbf{v}(\mathbf{C}) = \mathbf{M}\,(q_1^2, \ldots, q_m^2)^{\mathrm{T}}.$$

The condition number $\kappa = \kappa(\mathbf{M})$ measures the stability of this map (for any $m \geq 21$). The condition number is defined as the ratio of largest and smallest singular values of $\mathbf{M}$. This implies $\kappa \geq 1$ and $\kappa \to \infty$ if $\mathbf{M}$ does not have full rank (i.e., $\mathbf{M}\mathbf{M}^{\mathrm{T}}$ is not invertible). Numerical applications commonly prefer specification of the reciprocal condition number in order to have values in a finite interval. For the same reason we define the uniqueness number as

$$u(G) = \kappa(\mathbf{M})^{-1} \in [0, 1],$$

which has the following properties:

- $u(G)$ depends only on the shape of the mean glyph. It is a measure how well an arbitrary covariance matrix $\mathbf{C}$ can be reconstructed from sampling q on the mean glyph surface.
- $u(G)$ is invariant under rotation and scaling.
- $0 \leq u(G) \leq 1$. The larger $u(G)$, the better $\mathbf{C}$ can be reconstructed from sampling q.
- $u(G) = 0$ indicates that the glyph is not unique.

The uniqueness number depends on the number $m \geq 21$ of samples as well as on the sampling positions $\mathbf{g}_i$. Ideally we would like to compute

$$\inf\{\, u(G) \mid \text{given any possible sampling of } G \,\},$$

which is infeasible. However, *any* computed $u(G) > \varepsilon$ provides evidence of uniqueness for a suitable $\varepsilon \to 0$, and *any maximum* of computed values (e.g., for different samplings) gives an conservative estimate or a *lower bound* on uniqueness.

We illustrate these properties and the behavior of $u(G)$ in few numerical experiments: We start with 21 uniformly distributed random samples on the glyph surface and compute the uniqueness number. We observe that the particular sampling is generally not critical: the computed values of u typically do not vary much. As the uniqueness number depends on the selection of the sample points, one might be tempted to construct a "smart selection" or use "deterministic samples". We decided to use random samples because deterministic sampling would incorporate the orientation of the eigenvectors of $\bar{\mathbf{S}}$. This changes discontinuously in regions of equal eigenvalues, which leads to a violation of the continuity condition (3.) for glyph design. By incorporating additional samples, the number of rows in $\mathbf{M}$ typically increases, as this typically "adds" new information, and the condition number of $\mathbf{M}$ tends to decrease. This means the uniqueness number typically increases. The more samples, the less likely are additional samples to capture new information. Therefore uniqueness changes at a slower and slower rate and is expected to converge to a limit. This is illustrated in Figure 2a for the same mean tensor and two different glyph constructions. With a minimum at 21 values, $u(G)$ rises rapidly after including about 150 additional samples and remains stable from thereon.

Since $u(G)$ is independent of rotation and scaling, we can systematically compute $u(G)$ for all glyphs of a certain glyph type. For this, we consider the three eigenvalues of the mean glyph $\lambda_{1,2,3}$ as $\lambda_1 = 1$, $\lambda_{2,3} \in [-1, 1]$ and compute $u(G)$ for each $(\lambda_2, \lambda_3) \in [-1, 1]^2$. The resulting plot for the glyphs in [GRT17a] is shown in Figure 2b. It shows that $u(G) > 0$ if $\lambda_{1,2,3}$ are distinct and nonzero. Hence Figure 2b shows the uniqueness of the uncertain 3D glyphs of [GRT17a]. The height surface in Figure 2b was computed on a 151×151 sampling grid.

An uncertain glyph is considered to be unique for $u(G) > \varepsilon$ such that it is numerically clearly distinguishable from 0. In practice, we expect a significantly lower uniqueness for a close to minimal sampling ($m = 21$) than for higher m (see Figure 2a). However, even such cases correspond to condition numbers in the range of 10^5, which is perfectly tolerable for solving a linear system.

5.2. Intuitiveness

It remains to show that the field q on the mean glyph surface provides an intuitive encoding of uncertainty. This cannot be proven formally. Instead we motivate and explain intuition with help of few exemplary settings in 2D.

Figure 3 shows different visualizations of an ensemble of 2D tensors, which follow a given normal distribution. A 2D tensor can

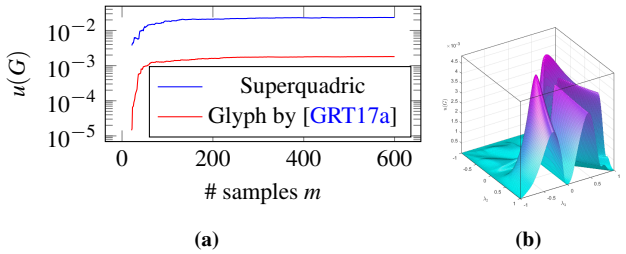

Figure 2: *(a) For an increasing number of samples on G, uniqueness u increases. The experiment shows random samples on the tensor* $\mathbf{v}(\bar{\mathbf{S}}) = (1, 0.5, 0.4, 0, 0, 0)^{\mathrm{T}}$. *For both choices of Q we observe a converging behavior of u. (b) Uniqueness* $u(G)$ *for different mean tensors using [GRT17a].* $\lambda_1 = 1$ *is fixed, and* $\lambda_2, \lambda_3 \in [-1, 1]$ *vary. The tensor is unique, if* $u(G) \neq 0$.

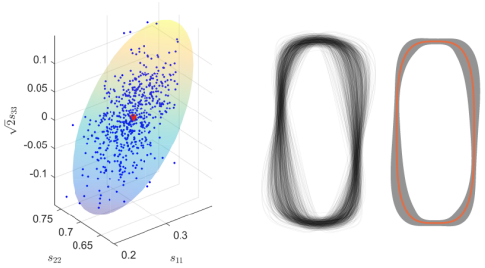

Figure 3: *Three visualizations of the same 2D tensor ensemble: as points in the vector space of tensor components* $\mathbf{s} = \mathbf{v}(\mathbf{S})$, *the red point denotes the mean tensor* $\bar{\mathbf{S}}$ *(left); as overlaid superquadric glyph curves (center); as uncertain glyph: mean* $G(\bar{\mathbf{S}})$ *is depicted as orange curve, the filled region is bounded by the outward/inward offset curves defined by q (right).*

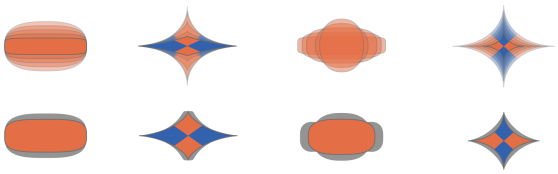

Figure 4: *Four different sets of tensor samples. Each set consists of 5 tensors that are generated by varying the eigenvalues (with constant eigenvectors). The top row shows overlaid superquadric glyphs. The bottom row shows our corresponding uncertain glyphs.*

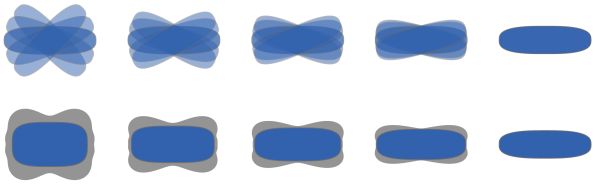

Figure 5: *Five different sets of tensor samples. Each set consists of 5 tensors that are generated by varying the direction of eigenvectors (with constant eigenvalues). The top row shows overlaid superquadric glyphs. The bottom row shows our corresponding uncertain glyphs.*

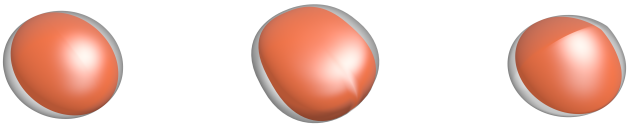

Figure 6: *Glyphs for uncertain tensor with* $\mathbf{v}(\bar{\mathbf{S}}) = (1, 0.8, 0.5, 0, 0, 0)^{\mathrm{T}}$, $\mathbf{C} = diag(0, 0, 0.2, 0, 0, 0)$. *The tensor varies in one principal direction. From left: ellipsoid glyph with* $u(G) = 0$, *superquadric glyph with* $u(G) \approx 9.1 \cdot 10^{-4}$, *glyph by [GRT17a] with* $u(G) \approx 1 \cdot 10^{-4}$.

be considered as a point in the 3-dimensional vector space of the tensor components $s_{11}, s_{22}, \sqrt{2}s_{12}$. Figure 3 (left) shows the tensors as 3D points. The red point denotes the mean tensor, and the overlaid ellipsoid denotes the covariance. Figure 3 (center) shows the same set of tensors by overlaying their corresponding transparent superquadric glyph surface (here: superellipses in 2D). We see that there are regions where many curves coincide, whereas in other regions there is a larger spread. Figure 3 (right) shows the same tensor ensemble with our visualization: the orange curve is a superquadric representation of the mean tensor, the field q is shown as the region bounded by offset curves in positive and negative normal directions. The relation to Figure 3 (center) is visually noticeable: In regions of high spread among the sampled glyph curves, the offset q is rather large. Figure 3 also shows that our glyph shows similarities with curve boxplots [MWK14], even though definition and properties are different.

To further study the meaning of the field q, we conduct the following experiment: We generate 5 samples of 2D tensors by varying properties in the spectral domain. Then we compute the best-fitting uncertain tensor by applying (4) and visualize its glyph. The top row of Figure 4 shows several collections of 5 tensors as overlaid superquadric glyphs. In the columns we vary (from left to right) 1. one eigenvalue (same signs), 2. one eigenvalue (opposite signs), 3. both eigenvalues (same sign) with inverse correlation, 4. both eigenvalues (opposite signs) with positive correlation of the magnitudes. The eigenvectors remain constant. The bottom row in Figure 4 shows the corresponding uncertain glyphs. The relation between the overlaid superquadric glyphs and our uncertain superquadric glyphs is clearly noticeable.

In Figure 5 we conduct the same experiment with constant eigenvalues and varying direction of eigenvectors. The amount of variation decreases from left to the right. The top row shows overlaid superquadrics, and the bottom row shows the corresponding uncertain glyphs. As before, the relation between the overlaid samples and the fitted distributions shown as uncertain glyphs is clearly noticeable.

We conduct similar experiments for 3D glyphs. Here, we compare different classes of glyphs that are extended to visualize uncertain tensors: simple ellipsoid glyphs (for positive-definite tensors), superquadric glyphs [SK10] and the glyphs presented by Gerrits et al. [GRT17a] (for the case of symmetric tensors). Figures 6 and 8

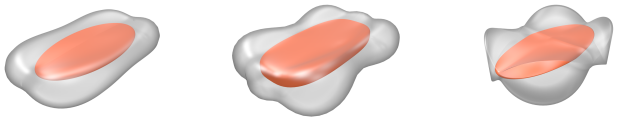

Figure 7: *Glyphs for uncertain tensor with* $\mathbf{v}(\bar{\mathbf{S}}) = (0.9, 0.7, 0.3, 0, 0, 0)^{\mathrm{T}}$ *and covariance that corresponds to varying plane rotation of eigenvectors. From left: ellipsoid glyph with* $u(G) = 0$*, superquadric glyph with* $u(G) \approx 3.4 \cdot 10^{-4}$*, glyph by [GRT17a] with* $u(G) \approx 2 \cdot 10^{-6}$.

Figure 8: *Glyphs for uncertain tensor with indefinite mean* $\mathbf{v}(\bar{\mathbf{S}}) = (1, 0.6, -0.5, 0, 0, 0)^{\mathrm{T}}$ *and* $\mathbf{C} = diag(0, 0.65, 0.03, 0, 0, 0)$*. The tensor varies in one principal direction. Left: superquadric glyph with* $u(G) \approx 1.5 \cdot 10^{-4}$*. Right: glyph by [GRT17a] with* $u(G) \approx 3 \cdot 10^{-6}$*. (There exists no ellipsoid glyphs in the indefinite case.)*

Figure 9: *Glyphs for uncertain tensor with*

$$\bar{\mathbf{S}} = \begin{pmatrix} 1 & 0.2 & 0.1 \\ 0.2 & 0.4 & 0.03 \\ 0.1 & 0.03 & 0.2 \end{pmatrix} \text{ and } \mathbf{C} = 10^{-3} \cdot \begin{pmatrix} 103 & 69 & 69 & 0 & 0 & 0 \\ 69 & 66 & 36 & 0 & 0 & 0 \\ 69 & 36 & 66 & 0 & 0 & 0 \\ 0 & 0 & 0 & 300 & 0 & 0 \\ 0 & 0 & 0 & 0 & 6 & 0 \\ 0 & 0 & 0 & 0 & 0 & 200 \end{pmatrix}.$$

From left: ellipsoid glyph with $u(G) = 0$*, superquadric glyph with* $u(G) \approx 3.6 \cdot 10^{-4}$*, glyph by [GRT17a] with* $u(G) \approx 5.3 \cdot 10^{-6}$.

show glyphs for ensembles with one varying eigenvalue, whereas Figure 7 shows glyphs for tensors that are varied by a plane rotation of eigenvectors. Figure 9 visualizes a randomly chosen uncertain tensor $(\bar{\mathbf{S}}, \mathbf{C})$. For each glyph we provide a uniqueness number $u(G)$ that was computed from a sampling at 21 random points on the glyph surface. We emphasize again, that this is no formal prove of intuitiveness but aims towards giving new insights into visualization of tensor uncertainty.

6. Results

We demonstrate how our new uncertainty glyph can be used as a tool for investigating uncertainty in tensor data by applying it to data from medical imaging as well as mechanical engineering. First, we apply our new tensor visualization to an ensemble of positive-definite symmetric diffusion tensor data given in the DTI multiple atlas set. The Human Brain Atlas was provided by the Johns Hopkins Medical Institute and the Laboratory of Brain Anatomical MRI. A horizontal slice is sampled for fourteen distinct members and a non-linear registration is applied on a rectangular grid as seen in Figure 10a. The measured tensors vary in magnitude and direction. We compute the mean tensor and covariance matrix for each sample location. Figures 10b to 10d show the superquadric tensor glyph visualization and the offset surface that indicates uncertainty. The produced glyphs allow to see the mean tensor throughout the ensemble members for all locations as well as the local uncertainty. Large offset surfaces indicate stronger variations among the members and provide a geometric insight of this variation. Glyphs shown at the bottom of Figure 10c encode a high uncertainty and show, that tensors vary in rotation. Especially tensor data measured close to the lateral ventricles show uncertainty.

Figure 11 shows one selected tensor of the same dataset. To illustrate the effect of uncertainty and its correspondence to derived uncertainty measures, we construct a traceless matrix $\mathbf{C}' = \mathbf{C} - \mathrm{diag}(\mathrm{trace}(\mathbf{C}))$ and use it as covariance matrix. The top row shows a blending $\alpha\mathbf{C}'$ with the zero matrix for $\alpha \in \{0, \frac{1}{4}, \frac{1}{2}, \frac{3}{4}, 1\}$. This increases uncertainty which is shown by the growing offsets. This offset is close to zero near the glyph axes that represent eigenvector directions. Note that visualizing only the trace of the covariance, which is often used as a derived uncertainty measure, would give the impression that all tensors are equal and certain. For the second row, we blend $\mathbf{C}'$ and the original covariance $\mathbf{C}$ stepwise from left to right as $(1-\alpha)\mathbf{C}' + \alpha\mathbf{C}$, which results only in a change of trace. This leads to an overall increase of the offset, also close to the axes. The overall volume of the surface allows for a quick understanding of the level of uncertainty, the glyphs however, also includes spatial information and indicates the type of uncertainty.

We further show the visualization of a stress tensor ensemble from static simulations of stresses applied to a steel cylinder. For the simulation, the bottom end geometry is fixed and rotational momentum is applied to each axis of the top end. While a mean rotation is applied to the longitudinal axis, three different additional torques are applied and varied for each simulation following a Gaussian distribution to form an ensemble of 10 different tensor fields where tensors are indefinite symmetric stress tensors. Again, a slice orthogonal to the mean rotation axis is sampled on a uniform grid to compute mean tensor and covariance matrix for each location and then visualized by applying our technique to the superquadric tensor glyph. The resulting image in Figure 12 clearly shows the rotational axis in the center of the slice, where the tensor vanishes. For most glyphs, the offset surface is close to the mean glyph surface, indicating a low uncertainty for the location. Only tensors at the left and right border show a stronger uncertainty, where eigenvalues vary while eigenvectors are stable.

Parameter discussion

While the scalar field q defined on the glyph surface is parameter free, its visual representation is not. A global scaling parameter of the glyph itself has been used to have the sampled tensors densely cover the area. Further, scaling the offset from the mean surfaces is possible to emphasize uncertainty but has not been used in this

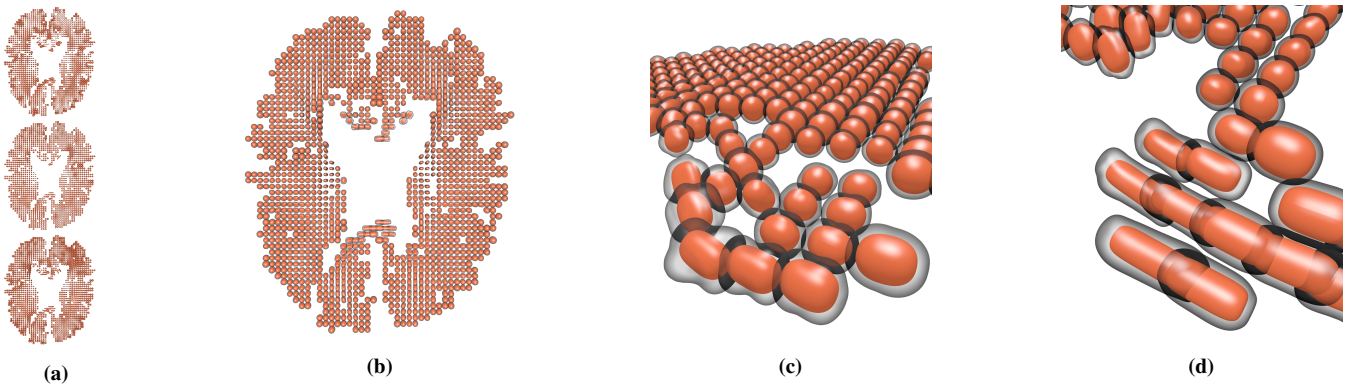

Figure 10: *Uncertain superquadric glyphs for an ensemble of Diffusion Tensor Imaging data of the human brain.*

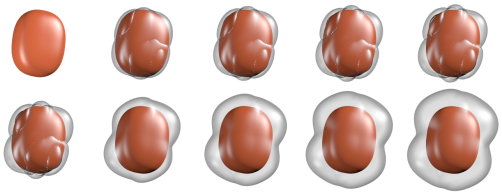

Figure 11: *Top: Linear blending of zero matrix and traceless matrix. Bottom: Linear blending of traceless matrix and original covariance matrix.*

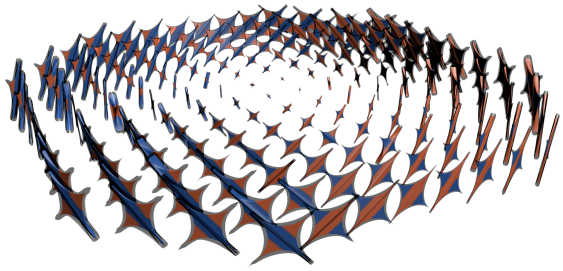

Figure 12: *Uncertain superquadric glyphs for an ensemble of simulated stress tensors from changing torque applied to a steel cylinder. The colors indicate the signs of eigenvalues, the transparent offset surfaces indicate uncertainty.*

work. As the offset surface is encasing the mean tensor, we chose opacity to solve the problem of overlapping. A suitable rendering needs to be applied such that shape and color of both, offset as well as mean surface can be perceived well. Other techniques for visualizing scalar fields on a surface might be applicable, as long as they do not lead to a violation of our wish list described in 2. Further parameters are related to sampling: When using finite differences to approximate derivatives, the step size between discrete points affects the accuracy. As described in 5.1, determining an uniqueness measure relies on sampling the glyph surface. For determining the uniqueness of the uncertain glyphs shown in Figures 6 to 9 we chose the minimum sample number of 21. Values in Figure 2b are computed for a selection of 600 samples to ensure the value is close to the tensors experimental limit.

Comparison to existing glyphs

To give a better understanding of how our contribution improves glyph visualization of uncertain tenors, we compare them with existing glyph techniques. As different mean tensors are affected differently by the same covariance, we compare our uncertain tensor glyphs to visualizations by [BP07] and [AWHS16]. As mentioned in Section 3, Basser et al. use a radial projection of mean and covariance tensors. Isosurfaces indicate mean tensor as well as standard deviation. Besides the visual complexity produced by three superimposed surfaces, the glyph construction cannot ensure unique representations. Due to the projection, mean tensors that only differ by the sign of eigenvalues will be mapped to the same scalar field. The same can be shown for the covariance, as only the totally symmetric part of the tensor is represented. Both mappings are not bijective. The bottom row of Figure 13 demonstrates this behavior: The surfaces for the mean tensor (shown in green) and standard deviation $\pm\sigma_{\text{std}}$ ($-\sigma_{\text{std}}$ red, $+\sigma_{\text{std}}$ blue) are superimposed and rendered translucent. Columns (a) and (b) show glyphs for the same mean tensor $\mathbf{v}(\bar{\mathbf{S}}) = (1,2,5,0,0,0)^{\mathrm{T}}$ but different matrices as covariance tensors. While the first matrix can be written as $\mathbf{C}_1 = \text{diag}(0,0,0,1,2,3)$, the second places the same non-zero values on different off-diagonal locations. The exact matrices can be found in the Appendix. Columns (a) and (c) show glyphs for the same covariance matrix but different mean tensors, as the sign of the minor eigenvalue is flipped such that $\mathbf{v}(\bar{\mathbf{S}}) = (-1,2,5,0,0,0)^{\mathrm{T}}$. The three resulting glyph visualization by [BP07] are identical, which is a violation of property (4.). In comparison, the top row shows our new glyphs for the same input tensors. They are clearly distinguishable and are capable to represent each combination uniquely.

Abbasloo et al. [AWHS16] visualize the impact on the mean tensor by decomposing the covariance into its eigentensors and rendering the effect of each eigenmode separately. They offer an animation to show how the mean tensor changes based on the different eigenmodes. Alternatively, these glyphs can be presented as overlays, to

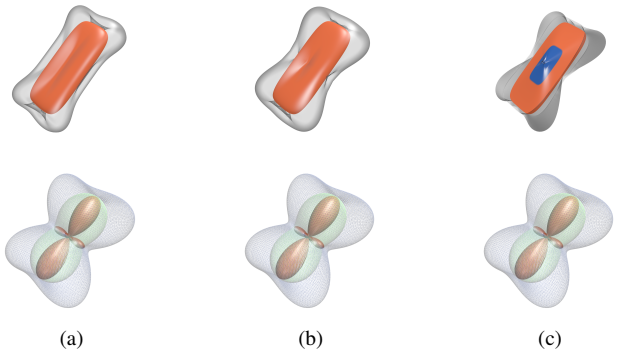

(a) (b) (c)

Figure 13: *Three different uncertain tensors visualized by our method (top row) and [BP07] (bottom row). While our method clearly shows different glyphs, the glyphs by [BP07] are identical: [BP07] is not unique.*

indicate confidence intervals of tensor distributions. The authors propose to add and subtract the eigentensor scaled by three times the corresponding eigenvalue to the mean tensor and render two superimposed superquadric glyphs. As the original mean tensor and thus its eigenvector directions are no longer visualized, this poses as a violation to property (5.). Eigentensors do, however, change in a discontinuous way when the covariance tensor is nearly isotropic, which leads to a sudden change in visualization even though the covariance tensors are virtually identical. This sudden change can be observed in Figure 14. Both (b) and (d) show visualizations for the same mean tensor $\mathbf{v}(\bar{\mathbf{S}}) = (1,2,5,0,0,0)^{\mathrm{T}}$. The six eigenvalues σ_i and eigentensors $\mathbf{E}^i$ extracted from the fourth-order covariance tensor are used to create six views. Each showing superquadric glyph representations for $\mathbf{D}_{\text{blue}} = \bar{\mathbf{S}} - 3\sigma_i\mathbf{E}^i$ and $\mathbf{D}_{\text{red}} = \bar{\mathbf{S}} + 3\sigma_i\mathbf{E}^i$ and labeled as eigenmode i. Note, that we used a simple translucent rendering of both glyphs, while [AWHS16] render both separately, adding a white core to areas where they overlap. For both covariance tensors used in (b) and (d), we use $\mathbf{C} = 0.3 \cdot \mathbf{I}$ and add random symmetric noise in the order of 10^{-8}. This slight noise leads to a sudden change in the eigentensors and therefore in the visualizations, which is a violation of the continuity property (3.). Our new glyph construction accounts for this problem. Uncertain tensor glyphs for the given tensors are shown in (a) and (c). The minimal change between both covariances results in a minimal change between both uncertain glyphs.

7. Future Research

Our approach opens future research in several directions:

Rendering. We distinguish surfaces G of the base glyph and the offset surface Q, which encodes uncertainty. Our current rendering style with solid surface for the mean tensor and a transparent surface for uncertainty is straightforward. More advanced rendering techniques are possible, which may be optimized towards a simultaneous perception of the shapes of both G and Q. This includes illustrative approaches, opacity optimization for surfaces [GSM*14] or a piecewise rendering [ZSL*16].

Optimal uniqueness sampling. While the current implementation relies on a random point sampling for computing uniqueness numbers, better sampling strategies may result in even smaller, i.e.better, uniqueness numbers for the uncertain glyphs. This, however, does not affect the actual glyph design or visualization, it only provides better information about uniqueness.

Extension to general (non-symmetric) tensors. For general 3D tensors we have 9 coefficients for the mean tensor and 45 of the covariance matrix. It seems to be challenging but not hopeless to extend our approach to general tensors.

8. Conclusions

The visualization of symmetric second-order tensors with uncertainty is a challenging problem: such tensors depend on 6 parameters in 3D, and the presence of uncertainty introduces another 21 parameters from covariance. This work presents – to the best of our knowledge – the first approach to direct visualization of uncertain tensors that incorporates *all* parameters in a single glyph. The new uncertain glyph is based on some standard glyph for certain tensors, which represents the mean tensor, and enriched by a scalar field that represents tensor covariance. As variance of intrinsic tensor properties can be derived from the covariance matrix, the full uncertainty information is encoded. The construction of the uncertain glyph respects important design properties for tensor glyphs, and provides a bijective map between the glyph and the uncertain tensor (i.e., mean tensor and covariance). This means that each uncertain tensor is assigned a unique glyph for a given class of standard tensor glyphs as basis. We derive formal criteria for uniqueness that can be used in formal proofs as well as for measuring "uniqueness" empirically for glyph instances. The empirical study is helpful because although the approach for proving or disproving uniqueness is simple (with help of lemma 1), the complexity of the formal expressions may "explode" if the basis glyph is defined w.r.t. a spectral basis. We demonstrate uncertain glyphs for a number of 2D and 3D examples. The visual comparison of the uncertain glyph for a best-fitting distribution with overlaid glyphs of the given ensemble members, indicates that the additional uncertainty can be encoded in a way that provides an idea of the given distribution. This is also emphasized by experiments where ensembles are generated by varying spectral parameters of the glyph. With this in mind, we believe that this work provides a valuable insight into encoding the effect of covariance on symmetric order tensors and the new glyphs provide a valuable tool for visual assessment of uncertain tensor data. This is demonstrated for a number of data sets.

Appendix

Rotations in tensor space

Given is a symmetric tensor $\mathbf{S} \in \mathbb{R}^{3\times3}$. For any rotation matrix $\mathbf{R}$ in (2) that acts on $\mathbf{S}$, the corresponding rotation $\hat{\mathbf{R}}$ that acts on $\mathbf{v}(\mathbf{S}) \in \mathbb{R}^6$ can be derived as

$$\hat{\mathbf{R}} = \begin{pmatrix} \mathbf{R}_{11} & \mathbf{R}_{12} \\ \mathbf{R}_{21} & \mathbf{R}_{22} \end{pmatrix} \quad \text{with}$$

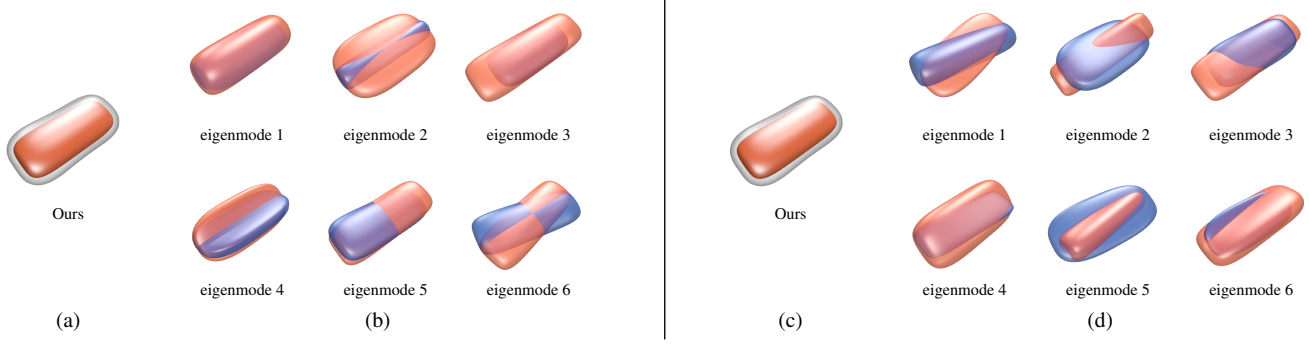

Figure 14: *Two almost identical uncertain tensors having almost identical glyphs by our method ((a) and (c)) but significantly different glyphs in the visualizations of [AWHS16] ((b) and (d)): [AWHS16] is not continuous.*

$$\begin{aligned}
\mathbf{R}_{11} &= \mathbf{R} \circ \mathbf{R} \\
\mathbf{R}_{21} &= \sqrt{2}\, \mathbf{R}_{(132)(123)} \circ \mathbf{R}_{(213)(123)} \\
\mathbf{R}_{12} &= \sqrt{2}\, \mathbf{R}_{(123)(132)} \circ \mathbf{R}_{(123)(213)} \\
\mathbf{R}_{22} &= 2\, \mathbf{R}_{(132)(132)} \circ \mathbf{R}_{(213)(213)} - \mathbf{R}_{(321)(321)} \,,
\end{aligned}$$

where $\circ$ denotes the entrywise Hadamard product of matrices and the subindices (ijk) denote permutations of matrix rows and columns, respectively. Note that [Hel94] provides a different construction based on plane rotations.

Sketch of Proof of Theorem 2

For the proof of theorem 2, we restrict ourselves to the 2D case. The basic idea is simple: provide 6 sample points on the glyph curve and show that they give a full rank matrix $\mathbf{M}$. The technical difficulty consists is the fact that the superquadric glyphs are parametrized in the spectral basis, whereas partial derivatives must be computed w.r.t. to the tensor components. We only give the (intermediate) results for derivations. Given is a symmetric positive definite tensor $\mathbf{S}$ and its spectral decomposition $\mathbf{S} = \mathbf{R}\Lambda\mathbf{R}^T$ where $\mathbf{R}$ is a rotation matrix with eigenvectors as columns, and $\Lambda = \left(\begin{smallmatrix} \lambda_1 & 0 \\ 0 & \lambda_2 \end{smallmatrix}\right)$ has the eigenvalues $0 < \lambda_2 \leq \lambda_1$ on its diagonal. Then the parametric representation of the glyph is

$$\mathbf{g}(\mathbf{S},\theta) = \mathbf{R}\Lambda \begin{pmatrix} \cos^\alpha\theta \\ \sin^\alpha\theta \end{pmatrix} \tag{19}$$

with $\alpha = \left(\frac{2\lambda_2}{\lambda_1+\lambda_2}\right)^\gamma$, $x^\alpha = \mathrm{sgn}(x)\,|x|^\alpha$, and $\gamma \geq 0$ serving as a shape parameter. W.l.o.g. we assume that $\mathbf{S}$ is diagonal, i.e., $\mathbf{R} = \mathbf{I}$. Note that this can always achieved by a change of the coordinate system. However, the main diagonal $\mathbf{S} = \Lambda$ generally has non-vanishing partials w.r.t. the off-diagonal entries s_{12}, because any (infinitesimal) change of the rotation results in a change of s_{12}.

We compute the gradient for the factors of $\mathbf{g}$ and summarize the results as

$$\begin{aligned}
\nabla_\mathbf{s}\mathbf{R} &= \left[\left(\begin{smallmatrix} 0 & 0 \\ 0 & 0 \end{smallmatrix}\right),\ \left(\begin{smallmatrix} 0 & 0 \\ 0 & 0 \end{smallmatrix}\right),\ \frac{\sqrt{2}}{2(\lambda_1-\lambda_2)} \left(\begin{smallmatrix} 0 & -1 \\ 1 & 0 \end{smallmatrix}\right) \right], \\
\nabla_\mathbf{s}\Lambda &= \left[\left(\begin{smallmatrix} 1 & 0 \\ 0 & 0 \end{smallmatrix}\right),\ \left(\begin{smallmatrix} 0 & 0 \\ 0 & 1 \end{smallmatrix}\right),\ \left(\begin{smallmatrix} 0 & 0 \\ 0 & 0 \end{smallmatrix}\right) \right], \\
\nabla_\mathbf{s}\alpha &= \tfrac{\alpha\gamma}{\lambda_1+\lambda_2} \left(-1\,,\ \tfrac{\lambda_1}{\lambda_2}\,,\ 0\right)^\mathrm{T}.
\end{aligned}$$

Note that these expressions are well defined only for $\lambda_1 \neq \lambda_2$ and $\lambda_1, \lambda_2 \neq 0$ as required in theorem 2. This gives

$$\nabla_\mathbf{s}\mathbf{g} = (\nabla_\mathbf{s}\mathbf{R}\,\Lambda + \mathbf{R}\,\nabla_\mathbf{s}\Lambda) \begin{pmatrix} \cos^\alpha\theta \\ \sin^\alpha\theta \end{pmatrix} + \mathbf{R}\,\Lambda\,\nabla_\mathbf{s}\alpha \begin{pmatrix} \cos^\alpha\theta\,\ln\cos\theta \\ \sin^\alpha\theta\,\ln\sin\theta \end{pmatrix}.$$

Now we select 6 sample points as

$$\mathbf{g}_i = \mathbf{g}(\mathbf{S}, i\frac{\pi}{6}) \quad \text{for} \quad i = 0,\ldots,5\,.$$

Then computing the gradients $\nabla_\mathbf{s}\mathbf{g}(\mathbf{S}, i\frac{\pi}{6})$ at the sample points, where common factors that are constant in $\mathbf{s}$ – they do not affect the rank of $\mathbf{M}$ – are dropped and some symmetries are exploited, gives sample vectors $\mathbf{q}_i$ of the form

$$(\mathbf{q}_1,\ldots,\mathbf{q}_6) = \begin{pmatrix} 1 & a & c & 0 & -c & -a \\ 0 & b & d & 1 & -d & -b \\ 0 & 1 & 1 & 0 & 1 & 1 \end{pmatrix} \tag{20}$$

for certain terms a,b,c,d, which depend on $\lambda_1,\lambda_2,\gamma$. Applying (17) (for the 2D case) to (20) gives

$$\mathbf{M} = \begin{pmatrix} 1 & a^2 & c^2 & 0 & c^2 & a^2 \\ 0 & b^2 & d^2 & 1 & d^2 & b^2 \\ 0 & 1 & 1 & 0 & 1 & 1 \\ 0 & \sqrt{2}ab & \sqrt{2}cd & 0 & \sqrt{2}cd & \sqrt{2}ab \\ 0 & \sqrt{2}a & \sqrt{2}c & 0 & -\sqrt{2}c & -\sqrt{2}a \\ 0 & \sqrt{2}b & \sqrt{2}d & 0 & -\sqrt{2}d & -\sqrt{2}b \end{pmatrix}.$$

Since $\det\mathbf{M} = 8\sqrt{2}\,f_1\,f_2$ with

$$\begin{aligned}
f_1 &= f_1(\lambda_1,\lambda_2,\gamma) = (ad - bc) \\
f_2 &= f_2(\lambda_1,\lambda_2,\gamma) = (ab - cd)\,,
\end{aligned}$$

$\mathbf{M}$ has full rank if neither f_1 nor f_2 vanish, which is the case. Instead of summarizing formal expressions for f_1, f_2 and a formal proof, we provide "visual evidence" that $f_1 f_2 \neq 0$: Figure 15 shows the functions f_1 and f_2 plotted as height fields for $\lambda_1 = 1$ in the range

$\lambda_2 \in [0,1]$ and $\gamma \in [0,2]$. It shows that f_1, f_2 do not vanish for $\gamma > 0$ and $0 < \lambda_2 < \lambda_1$.

Showing theorem 2 for the 3D case requires a sampling of 21 points on the glyph surface. The basic idea is same as for 2D, however, the involved expressions become significantly more complex.

8.1. Full matrices for experiment in Figure 13

The two matrices used as covariance tensors are given as

$$\mathbf{C}_1 = \begin{pmatrix} 0 & 0 & 0 & 0 & 0 & 0 \\ 0 & 0 & 0 & 0 & 0 & 0 \\ 0 & 0 & 0 & 0 & 0 & 0 \\ 0 & 0 & 0 & 1 & 0 & 0 \\ 0 & 0 & 0 & 0 & 2 & 0 \\ 0 & 0 & 0 & 0 & 0 & 3 \end{pmatrix}, \mathbf{C}_2 = \begin{pmatrix} 0 & 1 & 2 & 0 & 0 & 0 \\ 1 & 0 & 3 & 0 & 0 & 0 \\ 2 & 3 & 0 & 0 & 0 & 0 \\ 0 & 0 & 0 & 0 & 0 & 0 \\ 0 & 0 & 0 & 0 & 0 & 0 \\ 0 & 0 & 0 & 0 & 0 & 0 \end{pmatrix}.$$

Acknowledgments

This work was supported by DFG grant TH 692/13-1.

References

[AWHS16] ABBASLOO A., WIENS V., HERMANN M., SCHULTZ T.: Visualizing tensor normal distributions at multiple levels of detail. *IEEE TVCG 22* (2016), 975–984. 2, 3, 4, 9, 10, 11

[BHJ*14] BONNEAU G.-P., HEGE H.-C., JOHNSON C. R., OLIVEIRA M. M., POTTER K., RHEINGANS P., SCHULTZ T.: Overview and state-of-the-art of uncertainty visualization. In *Scientific Visualization*. Springer, 2014, pp. 3–27. 3

[BOL12] BRODLIE K., OSORIO R. A., LOPES A.: A review of uncertainty in data visualization. In *Expanding the frontiers of visual analytics and visualization*. Springer, 2012, pp. 81–109. 3

[BP03] BASSER P. J., PAJEVIC S.: A normal distribution for tensor-valued random variables: applications to diffusion tensor mri. *IEEE transactions on medical imaging 22* (2003), 785–794. 2, 3

[BP07] BASSER P. J., PAJEVIC S.: Spectral decomposition of a 4th-order covariance tensor: Applications to diffusion tensor MRI. *Signal Processing 87*, 2 (2007), 220–236. 2, 3, 9, 10

[GRT17a] GERRITS T., RÖSSL C., THEISEL H.: Glyphs for general second-order 2d and 3d tensors. *IEEE TVCG 23*, 1 (2017), 980–989. 1, 2, 3, 6, 7, 8

[GRT17b] GERRITS T., RÖSSL C., THEISEL H.: Glyphs for space-time jacobians of time-dependent vector fields. *Journal of WSCG* (2017). 3

[GSM*14] GÜNTHER T., SCHULZE M., MARTINEZ ESTURO J., RÖSSL C., THEISEL H.: Opacity optimization for surfaces. *CGF 33*, 3 (2014), 11–20. 10

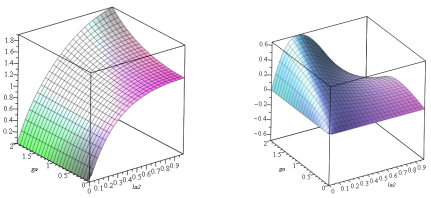

Figure 15: *The proof of theorem 2 involves two functions that must not vanish iff* $\mathbf{M}$ *has full rank. The plots visualize* f_1 *(left) and* f_1 *(right) for* $\lambda_1 = 1$ *in the range* $\lambda_2 \in [0,1]$ *and* $\gamma \in [0,2]$

[Hel94] HELBIG K.: Foundations of anisotropy for exploration seismics. In *Handbook of Geophysical Exploration: Seismic Exploration*, vol. 22. Elsevier, 1994, ch. Chapter 11 – Eigentensors of the elastic tensor and their relationship with material symmetry, pp. 393–470. 2, 11

[Jon03] JONES D. K.: Determining and visualizing uncertainty in estimates of fiber orientation from diffusion tensor MRI. *Magnetic Resonance in Medicine 49* (2003), 7–12. 3

[JPGJ12] JIAO F., PHILLIPS J. M., GUR Y., JOHNSON C. R.: Uncertainty visualization in hardi based on ensembles of ODFs. In *Visualization Symposium (PacificVis)* (2012), pp. 193–200. 3

[Kin04] KINDLMANN G.: Superquadric tensor glyphs. In *Proceedings of the Sixth Joint Eurographics - IEEE TCVG Conference on Visualization* (2004), VISSYM'04, Eurographics Association, pp. 147–154. 1, 3

[LP09] LÖFFLER M., PHILLIPS J. M.: Shape fitting on point sets with probability distributions. In *Algorithms – ESA* (2009), Fiat A., Sanders P., (Eds.), Springer, pp. 313–324. 3

[MWK14] MIRZARGAR M., WHITAKER R. T., KIRBY R. M.: Curve boxplot: Generalization of boxplot for ensembles of curves. *IEEE TVCG 20*, 12 (2014), 2654–2663. 7

[SK10] SCHULTZ T., KINDLMANN G. L.: Superquadric glyphs for symmetric Second-Order tensors. *IEEE TVCG 16*, 6 (2010), 1595–1604. 1, 2, 3, 7

[SK16] SELTZER N., KINDLMANN G.: Glyphs for asymmetric second-order 2d tensors. *CGF 35*, 3 (2016), 141–150. 3

[SSSSW13] SCHULTZ T., SCHLAFFKE L., SCHÖLKOPF B., SCHMIDT-WILCKE T.: Hifive: A hilbert space embedding of fiber variability estimates for uncertainty modeling and visualization. *CGF 32*, 3 (2013), 121–130. 3

[ZCH*17] ZHANG C., CAAN M., HÖLLT T., EISEMANN E., VILANOVA A.: Overview + detail visualization for ensembles of diffusion tensors. *CGF 36*, 3 (2017), 121–132. 2, 3

[ZSL*16] ZHANG C., SCHULTZ T., LAWONN K., EISEMANN E., VILANOVA A.: Glyph-based comparative visualization for diffusion tensor fields. *IEEE TVCG 22*, 1 (2016), 797–806. 2, 10